Available online at www.sciencedirect.com
SCIENCE DIRECT
International Journal of Heat and Mass Transfer 49 (2006) 3462–3476
International Journal of HEAT and MASS TRANSFER
www.elsevier.com/locate/ijhmt

Flow structure and heat transfer in a lower half heated and upper half cooled rectangular enclosure

Hongmin Li *, Minel J. Braun, Govind Paudel

Department of Mechanical Engineering, The University of Akron, Akron, OH 44325, USA

Received 26 August 2005; received in revised form 28 February 2006
Available online 15 June 2006

Abstract

This paper presents an experimental and numerical investigation on the natural convection in a rectangular enclosure with lower-half-heated, upper-half-cooled sidewalls. The flow structure contains thin wall-layers and large central vortical circulating zones. The mixing process and the fluid paths caused by the wall-layer head-on collisions and stream–stream interaction are fundamental to the development of the heat and fluid transport mechanisms. The understanding of the flow structures and their mutual interaction provides a guide leading to the optimization of the autoclave internal architecture and to practical suggestions for the design strategy of crystal growth vessels.

Keywords: Enclosure; Convection; Autoclave; Thermosyphone; Transport; Mechanism

1. Introduction

Natural convection flow and heat transfer in enclosures have been the focus of numerous studies. Comprehensive reviews have been offered by Canton [1] and Ostrach [2,3]. Most of the research work concentrated on modeling the flows for energy efficiency optimization in building structures, fire control, and solar energy utilization. Among these studies, which cover a wide range of fixed enclosure aspect ratios, there are three kinds of heating configurations of the enclosure walls: (i) heating and cooling come from the two sidewalls with the driving temperature gradient perpendicular to the direction of gravity, while the top and bottom walls are adiabatic, or conductive, (ii) the bottom wall of the enclosure is heated, and the top wall is cooled; they are both maintained at constant temperature, or under constant heat flux; the driving temperature gradient is parallel to that of gravity, while the sidewalls are adiabatic or conductive, and (iii) a combination of both horizontal and vertical temperature gradients. Some other studies dealt with specially modified geometries that actually represent variations of the first two cases mentioned above [4–8]. One well-studied case of the third configuration is that of an enclosure tilted relative to the gravity vector [9,10]. The two sidewalls, which have different temperatures, establish a temperature gradient with both horizontal and vertical components over the whole enclosure. Another case of the third configuration is that of lower-half heated and upper-half cooled cylindrical or rectangular enclosures [11,12].

The thermosyphones technology [13–15] and the autoclaves for hydrothermal crystal growth [16–18] are two of the industrial applications for flow in enclosures with lower-half-heated, upper-half-cooled sidewalls. The heating and cooling on the sidewalls establish the temperatures in the upper and lower regions of the enclosure. Most of the studies of flow in thermosyphones were performed in the steady-state laminar flow regime. For hydrothermal growth vessels, the two temperature zones drive the dissolving of the raw material and the growing of the seeds. The natural convection flow, thus established, carries the mass from the raw material region to the seed region.

* Corresponding author. Tel.: +1 330 329 0051; fax: +1 330 972 6027.
E-mail address: HL3@uakron.edu (H. Li).

0017-9310/$ - see front matter © 2006 Elsevier Ltd. All rights reserved.
doi:10.1016/j.ijheatmasstransfer.2006.02.054

The flows during hydrothermal crystal growth cover regimes from steady laminar to highly turbulent flows with Rayleigh numbers ranging from 10^4 to 10^{12} [19,20]. Various investigations have been carried out by the present authors for the highly turbulent flows [16–18]. The numerical simulations with turbulence models provide only time-averaged quantities for the fluctuating variables, which in turn present only a time-averaged fluid and heat transport mechanism, [16,18]. Flows in the unsteady laminar and transitional regimes, however, are not well studied and the corresponding flow structures and heat transfer process are neither well understood, nor widely documented in the literature. One also has to mention at this juncture that most measurements in the industry of the hydrothermal growth vessels are qualitative. To date, there is no quantitative data published in the literature suitable for numerical model validation.

2. Scope of work

In this paper we shall study both experimentally and numerically the natural convection flow in an enclosure that reproduces the type of thermal environment characterizing an autoclave, albeit not at the same temperatures and pressures. The model provides hot lower-half, and cold upper-half sidewalls and a Rayleigh number that characterizes an actual autoclave working in the unsteady laminar flow regimes. The flow structures and temperature distributions are visualized and then compared with the numerical simulation. The fluid exchange mechanism and flow interaction are studied and related to the application on hydrothermal crystal growth. The Raleigh number provides valid dynamic similarity. The latter, combined with the geometric similarity of the enclosure provides full scalability of the experimental/numerical results to the real world of the industrial applications. Validation of the numerical model will allow its further usage with significant confidence for thermal and pressure ranges not reproduced in the laboratory.

3. The experimental facility

3.1. Experimental system

A schematic of the experimental system is shown in Fig. 1. The system contains a test section connected to a set of two circulating baths which supply constant high-temperature water at T_H to two lower and opposite side heaters and constant low-temperature water at T_L to two upper and opposite side heaters, respectively. For each pair of heaters, the same water flow rates are maintained by using connecting tubes networks with the same flow resistance. The test enclosure manufactured out of clear Lucite is sandwiched between the two lateral sets of heaters. Two different sets of lighting sources are used in this work. The laser based system (shown in Fig. 1) is used to visualize in detail the flow patterns, while a white-light source is used in conjunction with thermochromic liquid crystals (TLC) to visualize non-intrusively the full temperature field in the bulk core and wall-layers of the fluid. Both the laser coherent and the diffuse white light beams are turned into thin sheets of light that define precise planes of investigation in the fluid. A photo-camera or a video-camera is focused on the light plane and used to record the flow and temperature patterns. The techniques and procedures are described at length by Braun et al. [21–23], Dzodzo et al. [24], and Lattime [25].

3.2. Laser and white light vision system

The laser based vision system, used for flow patterns and velocity measurements, contains a high-power, 5 W,

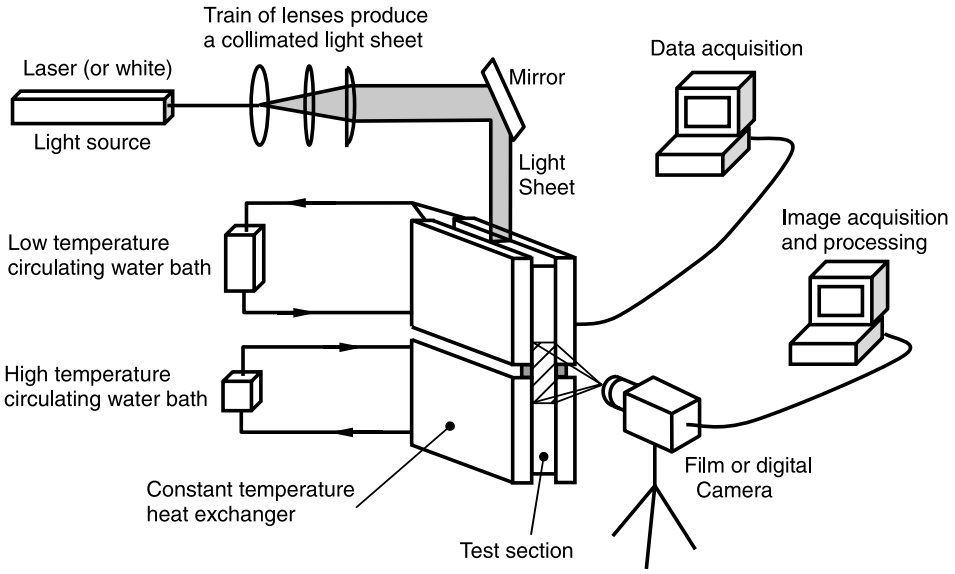

Fig. 1. Schematic of the experimental system.

Argon-Ion, blue-green continuous wave laser, a combination of cylindrical and spherical lenses that transform the cylindrical beam of light into a light sheet that is approximately 0.5 mm (0.020 in.) thick, and a computer based image recording system. A modified black and white digital Pulnix video-camera allows either interlaced or non-interlaced viewing of the illuminated plane in the fluid, at a frequency of 30 Hz. The camera has attached to it a lens system that has been configured as a long distance microscope, thus simultaneously allowing both a large working distance (10–25 in./254–635 mm) and high magnification (up to ×400). The images of fluid flow, which is seeded with 5–20 μm magnesium oxide particles, were recorded in a digital non-interlaced format. The images are computer-processed to obtain the velocity field data.

A true white-light source is used in place of the laser for visualization of the TLC particles that change color with temperature. The train of lenses previously used is now slightly modified to accommodate the "diffuse" light and the larger diameter (approx 0.8 in, 20 mm) beam. A Fuji-Film FinePix SPro digital camera and a combination of low luminosity high magnification Nikon lenses are used to record the color photos of the temperature field.

3.3. The test section

The configuration of the test section is shown in Fig. 2. The central section is a clear Lucite box, 368 mm high × 216 mm wide × 89 mm thick. The wall thickness is 13 mm. The inside surfaces of the bottom and back walls are painted flat black to reduce light reflection and glare and obtain high contrast quality black and white and especially color images. The box is sandwiched between the two sets of flat surface heat exchangers (HE) described earlier

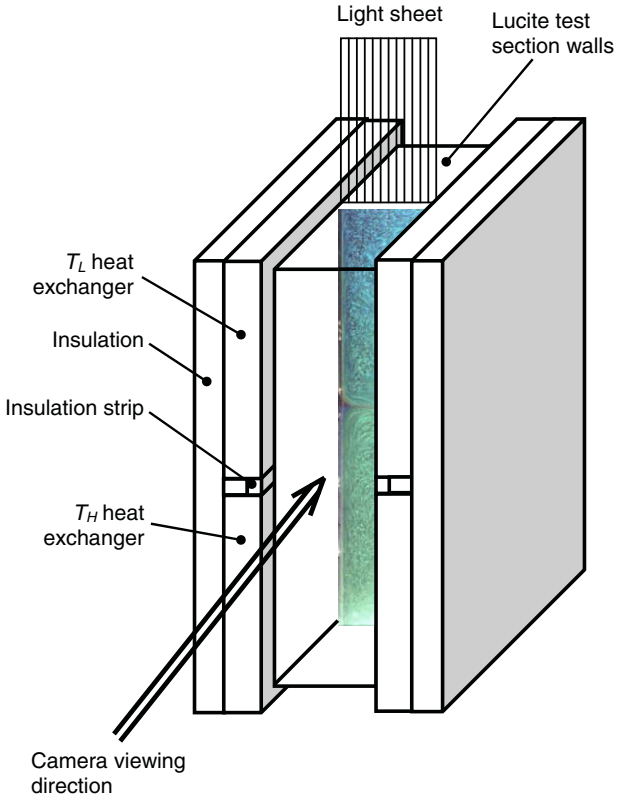

Fig. 2. Schematic of the test section.

that provide the flow driving temperature differentials. The upper and lower sets of HEs are separated 13 mm apart by ceramic insulation strips that reduce direct heat losses between the hot and cold HEs (see Fig. 2, also CC′E′E and DD′F′F in Fig. 3). The HEs are lined up with insulation on their air-exposed sides in order to eliminate

Boundaries	Conditions
ABB'A', GHH'G'	Adiabatic
ABHG, A'B'H'G'	Adiabatic
AA'C'C, BB'D'D	Wall at T_L
CC'E'E, DD'F'F	Adiabatic
EE'G'G, FF'H'H	Wall at T_H

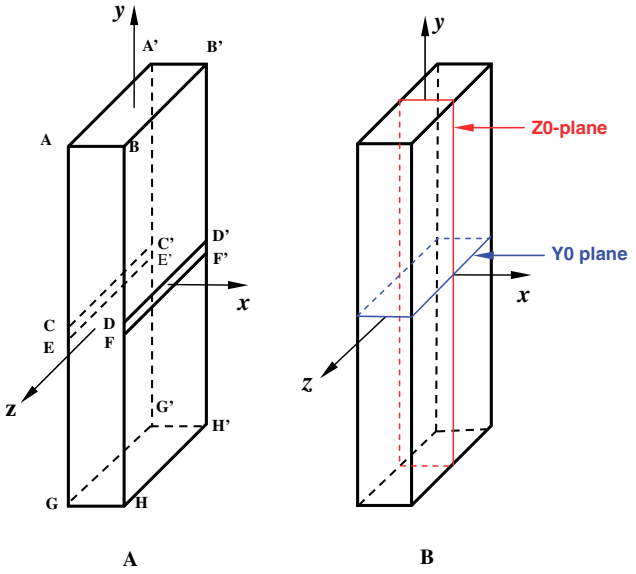

Fig. 3. Schematic of the domain and boundary conditions of the three-dimensional numerical model: (A) the model geometry and boundaries and (B) visualization planes.

heat loss to the environment. In order to monitor the temperatures on the liquid exposed surfaces of the HEs, flat film thermocouples (1.57E−2 mm thick) were installed. The location of the thermocouples and a discussion of the temperature distribution on the HE surfaces can be found in previous studies [14,19]. In this study the temperature T_H of the lower HEs, and the temperature T_L of the upper HEs, are set and controlled to be 32.5 °C and 28.5 °C respectively. With the above T_H and T_L, a 4 °C flow driving temperature difference is established between the lower and the upper walls.

4. The numerical model

A three-dimensional (3-D) model is developed for the simulation of the flow using the surface temperatures measured during the experimental program as boundary conditions. Fig. 3A presents the graphic representation of the test section enclosure in its 3-D embodiment while Fig. 3B shows the cross-sectional planes ($Y0$ and $Z0$), on which experimental and numerical flow and temperature distributions will be presented. Every surface that represents a boundary to the fluid domain is lettered as shown in Fig. 3. Due to their low thermal conductivity, the top and bottom walls (ABB′A′ and GHH′G′), as well as the vertical enclosure walls, ABHG and A′B′H′G′ are considered to be adiabatic. The full Navier–Stokes and energy equations are solved interactively in a feedback mode. In vector format, the full governing equations are given by Eqs. (1)–(3).

$$\nabla \vec{U} = 0 \tag{1}$$

$$\frac{\partial \vec{U}}{\partial t} + \vec{U} \cdot \nabla \vec{U} = \frac{1}{\rho} \operatorname{grad} P + \nu \nabla^2 \vec{U} + \vec{F} \tag{2}$$

$$\frac{\partial T}{\partial t} + \vec{U} \cdot \nabla T = \frac{k}{\rho \cdot C_p} \nabla^2 T \tag{3}$$

The driving buoyancy force, $\vec{F} = g \cdot \beta \cdot (T - T_0)$ where g is the gravity, is oriented in the positive y-direction due to the nature of the coordinate system (Fig. 3A). In this study, $T_0 = (T_H + T_L)/2$ is introduced as a reference temperature. The above equations are solved for the geometry shown in Fig. 3A, the boundary conditions listed in Fig. 3, and the fluid properties given in Table 1. Based on the enclosure width, W, the Ra number, $Ra_W = \frac{g \cdot \beta \cdot \Delta T \cdot W^3}{\nu^2} Pr$, used in this study is 1.1×10^7. This value is indicative of either an unsteady laminar, or a transitional flow regime for the enclosure and heating configuration described above [19].

Table 1
Fluid properties used in the numerical models (properties of water at 30.5 °C and 1 atm)

Properties	In SI units
Density, ρ	996
Viscosity, μ	7.977×10^{-4}
Thermal expansion coefficient, β	3.05×10^{-4}
Conductivity, k	0.6155
Heat capacity, C_p	4183

Table 2
Grid independence obtained for the numerical model

Grid	Grid size (xyz)	Total heat flow rate, Q_i (W)	Difference $\lvert Q_i - Q_{i+1}\rvert / Q_{i+1}$
Grid (a)	$120 \times 150 \times 70$	$Q_1 = 53.82$	0.83%
Grid (b)	$80 \times 110 \times 50$	$Q_2 = 54.27$	4.2%
Grid (c)	$40 \times 55 \times 25$	$Q_3 = 56.62$	6.7%
Grid (d)	$20 \times 33 \times 15$	$Q_4 = 60.71$	

The numerical solution uses a finite-volume based algorithm. The unsteady flow solution uses a time marching technique with a time step of 0.02 s. The discretization of the momentum and energy equations employs a second order upwind scheme for increased computational accuracy. The residuals of continuity, momentum, and energy equations are lower than 10^{-6}, 10^{-4}, and 10^{-6} respectively, for each time step convergence. The under-relaxation factors for mass and momentum equations are 0.4 and 0.5 respectively.

To evaluate the convergence of the numerical results, a set of grid convergence studies were performed. Based on the experimentally visualized flow structures, two parameters, instead of one overall parameter, were selected to compare the results when grid density was gradually increased. The two parameters are: (i) the heat flow rate from the lower walls, Q, and (ii) the velocity fluctuation in the center region. The first parameter is measuring convergence looking at the global parameter Q, which is the result of the integration performed over the entire control surface. The second parameter however, is a local measure of convergence. The convergence experiments used four sets of grids: (a) $120 \times 150 \times 70$, (b) $80 \times 110 \times 50$, (c) $40 \times 55 \times 25$ and (d) $20 \times 33 \times 15$, respectively. Grid independence, for both of the above mentioned parameters, was achieved with grid (a) configuration. The total heat flow rates obtained with these grids are presented in Table 2. Thus, the results presented henceforth are all based on the Grid (a) density.

5. Results and discussion

5.1. Calibration of the thermochromic liquid crystal (TLC) particles

In this study, microencapsulated TLC particles are used to visualize and quantify the temperature field associated with the fluid motion. Pure thermochromic liquid crystal materials are thick, oily, viscous liquids. For practical applications, the TLC mixtures are subject to individual droplets of liquid crystal microencapsulation. The microcapsule is a tiny droplet of liquid crystal surrounded by a thin polymer coating. Encapsulated TLC can thus be used in fluids where the microcapsules keep their discrete identi-

ties. The microcapsules used in this study are of chiral-nematic type with a time response in the range of 5–10 ms (versus that the cholesteric type microcapsules respond in 50–100 ms) [26]. The color play, as well as the event temperature range of TLC can be selected by adjusting their composition. TLC mixtures are identified by a color play code, which represents the range of colors that the TLC capsules reflect while in their temperature range. The code generally begins with the red or mid-green starting temperature. Next, the code defines the effective temperature band. The code for the chiral-nematic TLC used in this experiment is R28C4W.

Details of the application of TLC on temperature visualization can be found in Refs. [25,27,28]. For a specific set of TLC particles, the relation between the temperature and the color (hue value) is unique and depends on the TLC active range, the CCD camera sensors, lens quality, and the type of the light source. All these components are brought together in the calibration procedure whose final product is the temperature-hue value curve shown in Fig. 4. This curve is then used to produce an electronic color bar that allows the conversion of the raw hue information read by the CCD sensor to quantitative temperature data. The electronic color bar is fundamentally a color processing and recognition computer algorithm. As mentioned, the active temperature range of the microencapsulated TLC particles is 4 °C. That is, they become active with a red hue at the lower limit of the range and then go through the colors of the spectrum. When the activity band is exhausted, their color is a dark blue. This TLC with a narrower temperature band was chosen to ensure the accuracy of the temperature measurement in the thin upper wall-layers of the enclosure. Experimental practice found that for the hue values between 0 and 220 corresponding to a 2 °C temperature band from 28.5 °C to 30.5 °C, accurate temperature data can be successfully obtained. The temperatures in the upper wall-layers fall in such a temperature band. In the core of the enclosure the hue is above 220 and while a hue for temperature evaluation exists, the uncertainty in the measurement is too high for an accurate evaluation of the thermal map of this region.

The calibration system, which has been described in detail by Braun [21], Dzodzo [24] and Lattime [25], consists of a 25 mm × 25 mm × 25 mm cubic enclosure with two surface heat exchangers forming its top and bottom walls. This is a classical arrangement that has been widely described in the natural convection literature. One water bath supplies the same constant temperature water to both heat exchangers. The enclosure is well insulated on all sidewalls with exception of two situated at 90° with each other: one for the light sheet entry, the other for the camera field of view. With this setup, a constant temperature can be reached in the fluid inside the enclosure. A Chromel–Alumel K-type thermocouple is located at the center of the enclosure. Note that under these thermal conditions there is no fluid circulation and/or stratification. The digital camera is focused on the region around the thermocouple bead. The hue values of the TLC are obtained from the digital picture, and then are associated with the thermocouple reading. The average of the hue values at the read temperatures and their standard deviation are given in Fig. 4. The K-type thermocouple used here had an uncertainty of ±0.1 °C. We used a least squares regression method to correlate the TLC hues to their corresponding temperatures. This calibration curve was then used to query the digital image hue for the conversion to temperature. Fig. 4 shows the calibration data points and corresponding polynomial regressions which were fitted to the data for the type of TLC used in this work. The figure shows well correlated fits for the first regression curve with standard error estimates at or below 0.12 °C. This first region corresponds to the

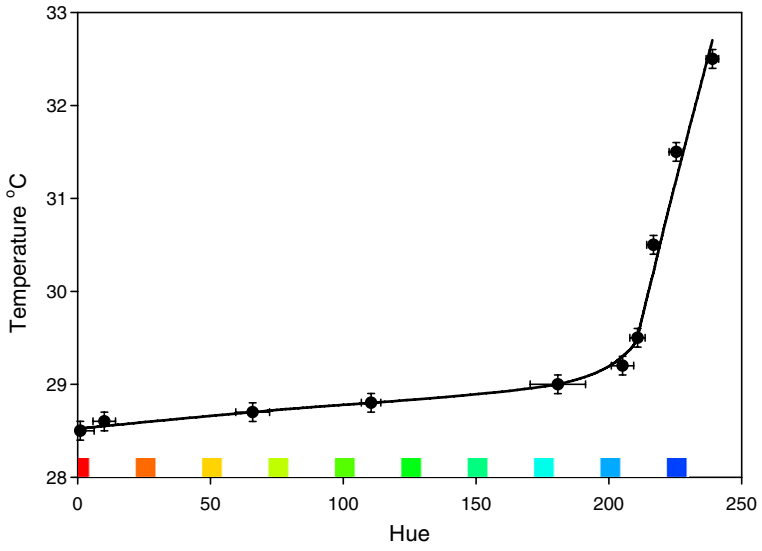

Fig. 4. Calibration curve of the thermal chromic liquid crystal particles.

"red to light blue" color band which covers the 28.5 °C to 30.5 °C (or hue value ranging from 0 to 220). The second region of the graphs, which represent the "light blue to dark blue" of the color band, covers hue values above 220, shows a drastic slope and a much poorer correlation fit to the polynomial regression. Data acquired outside the range the 0–220 hue is suspect to a degree of uncertainty high enough to prevent us from using it for quantitative temperature evaluation. However, one can still observe a blue hue as long as the temperatures are below 32.5 °C, and a qualitative evaluation of the core temperatures is still possible.

5.2. Overall flow structure

The overall experimental and numerical flow patterns obtained in the plane $Z0$ are shown in Figs. 5 and 6, respectively. Fig. 5 shows the experimental flow images at different time intervals with the exposure time of 4 s, while Fig. 6 shows numerically simulated flow patterns realized using the boundary conditions from the experimental undertaking. One needs to remark here that the images of Fig. 5 and the flow patterns of Fig. 6 are representative sets of the typical, repetitive flow structures observed in the enclosure. One can see that generally the flow structure contains

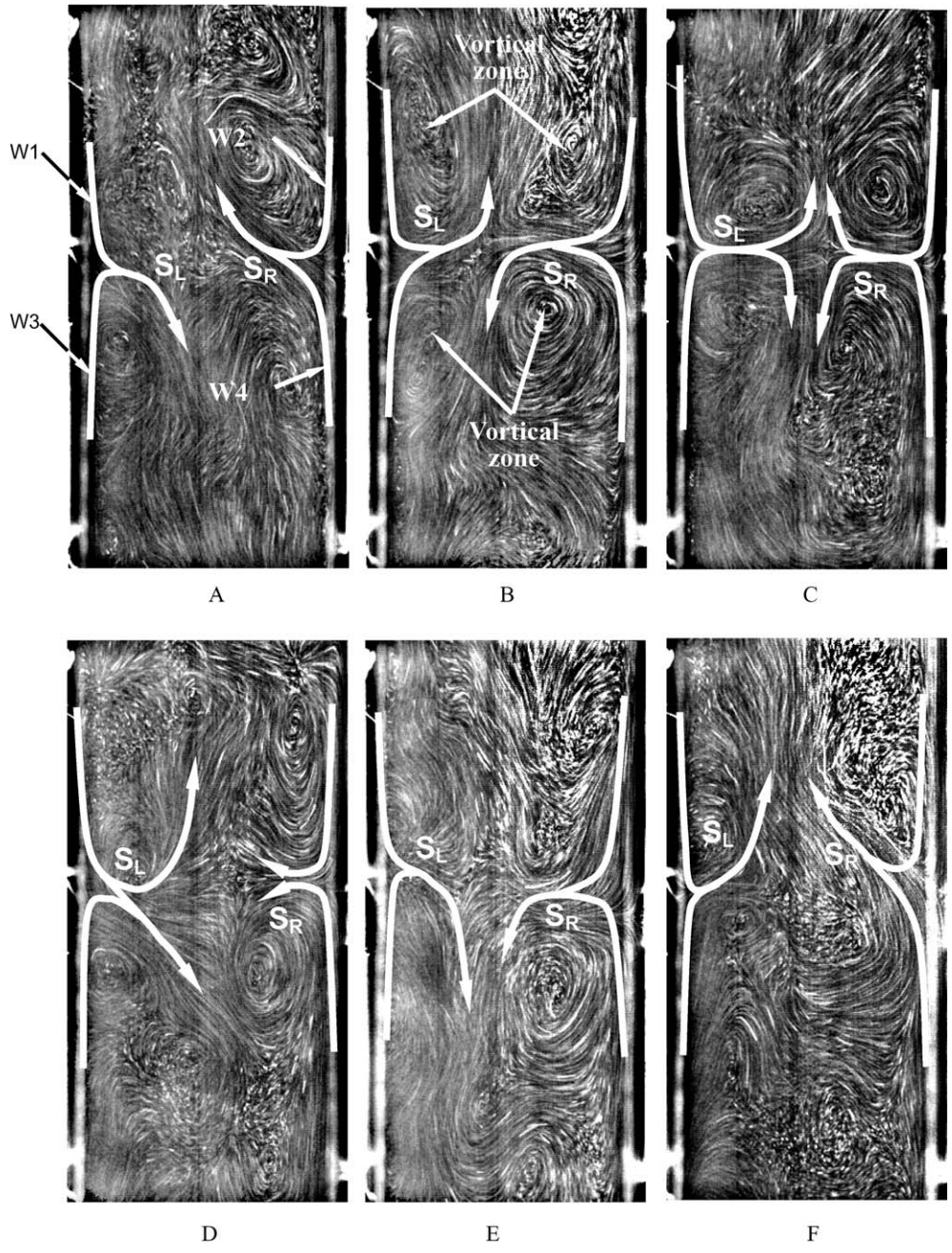

Fig. 5. Experimental flow structure images in $Z0$-plane with $\Delta T = 4$ °C. W1 and W2 are downward moving wall-layers. W3 and W4 are upward moving wall-layers. S_L and S_R are the streams formed by wall-layers.

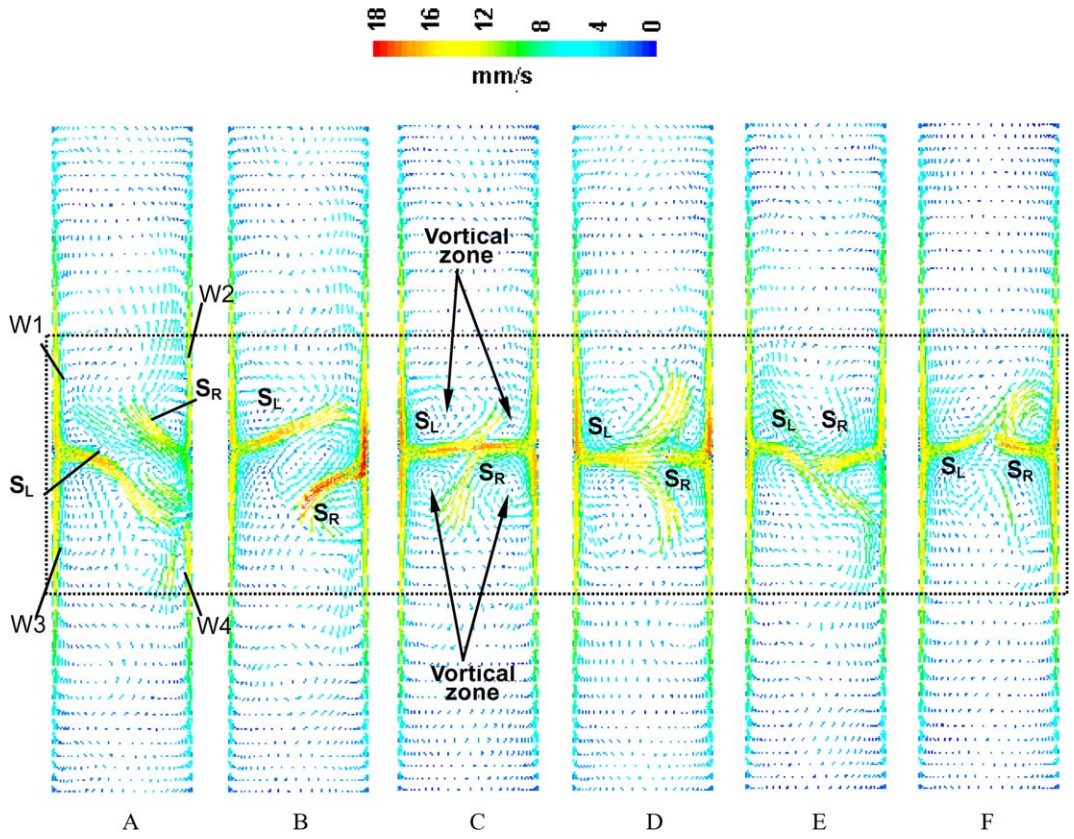

Fig. 6. Numerically simulated flow structures in the $Z0$-plane with $\Delta T = 4$ °C. W1 and W2 are the downward moving wall-layers. W3 and W4 are the upward moving wall-layers. S_L and S_R are the streams formed by wall-layers.

four wall-layers, W1 through W4, and two crossover streams marked as S_L and S_R. Regions W1 and W2 are wall-layers moving downward along the upper sidewalls, while W3 and W4 are wall-layers moving upward along the lower sidewalls. A study of the internal flow reveals that stream S_L is born through the interaction of wall-layers W1 and W3. Accordingly, stream S_R is formed by the interaction of wall-layers W2 and W4. These crossover streams fill out and flow in the core region bounded by the wall-layers. Flows in the wall-layers appear to be space- and time-wise steady, while streams S_L and S_R are fundamentally unsteady, but repetitive (a quasi-steady behavior) in nature at the $Ra_w = 1.1 \times 10^7$ used in this study. Note that the thickness and volume of the wall-layers is small compared to the width of the enclosure and the volume of the central streams. The latter entrain easily distinguishable vortical zones both in the upper and lower halves as marked in Figs. 5C and 6C; these formations can be followed in all other flow images of Figs. 5 and 6. In the vortical zones, flow is unsteady but repetitive, and the mixing patterns are complicated, especially due to the collision of wall-layers with different thermal content. The lower temperature fluid from the upper wall-layers interacts with the higher temperature fluid from the lower wall-layers. In Figs. 5A (experimental) and 6A (numerical), one can see that S_L flows into the lower half while S_R into the upper half. In Figs. 5B and 6B, however, the same stream formations flow in opposite directions: S_L into the upper half, while S_R into the lower half. In Figs. 5C and 6C, the S_L and S_R streams have a head-on collision at the center. By the extent of the S_L and S_R regions, it appears that the two streams have similar momentum strength. However, in Figs. 5D and 6D, the stream S_L has a higher strength than S_R and the location of the head-on collision is thus shifted towards the side where the stream is weaker. In Figs. 5E and 6E both S_L and S_R streams are headed towards the lower half, while in Figs. 5F and 6F, the two streams have reversed course, and are headed towards the upper half. The flow patterns in Figs. 5E and F, and 6E and F respectively appear, at a first inspection, to not satisfy the continuity. However, one has to keep in mind that this is a three-dimensional flow, and that the flow in the third z-direction, perpendicular to the $Z0$-plane was not visualized here. That mass flow however, provides the key to overall mass conservation. The structure of flow streams in the z-direction (three-dimensional structure) will be discussed later-on in the paper.

Each component of the flow structure described above is quasi-cyclic in nature, that is, the flow direction of either streams is alternating, but not at a constant time interval, and the time between the flow switches from one pattern to another is not regular either. However the patterns are repetitive. Finally, vortices are generated by these unsteady flow streams. The length scale of the vortices, or the sizes of

the vortexes are clearly of the same order of magnitude as the width of the chamber. During these experiments we have not witnessed cascades of vortex length scales from big to small. By examining the experimental flow images of Fig. 5 and the corresponding numerically simulated flow patterns of Fig. 6, one can ascertain that the flow behavior in both the wall-layers and the cores is well reproduced by the numerical model. Thus, one can certify with confidence the use of this numerical model in further parametric studies (parameters: higher temperature differences, different fluid density, other enclosure aspect ratios) of the natural convection.

5.3. Overall temperature profile

The temperature profiles obtained experimentally with the TLC particles and their corresponding numerical simulations are shown in Figs. 7 and 8 respectively. The photographs in Fig. 7, present the original color images taken at sequential and equally spaced z-cross-sections parallel to the $Z0$-plane. The exposure time of 2 s allowed not only to assess the color of the TLC but also to visualize/trace the associated flow trajectory. The photographs of the planes on the backside of the box, Fig. 7F and G, are darker compared to the photos of the front planes (Fig. 7A

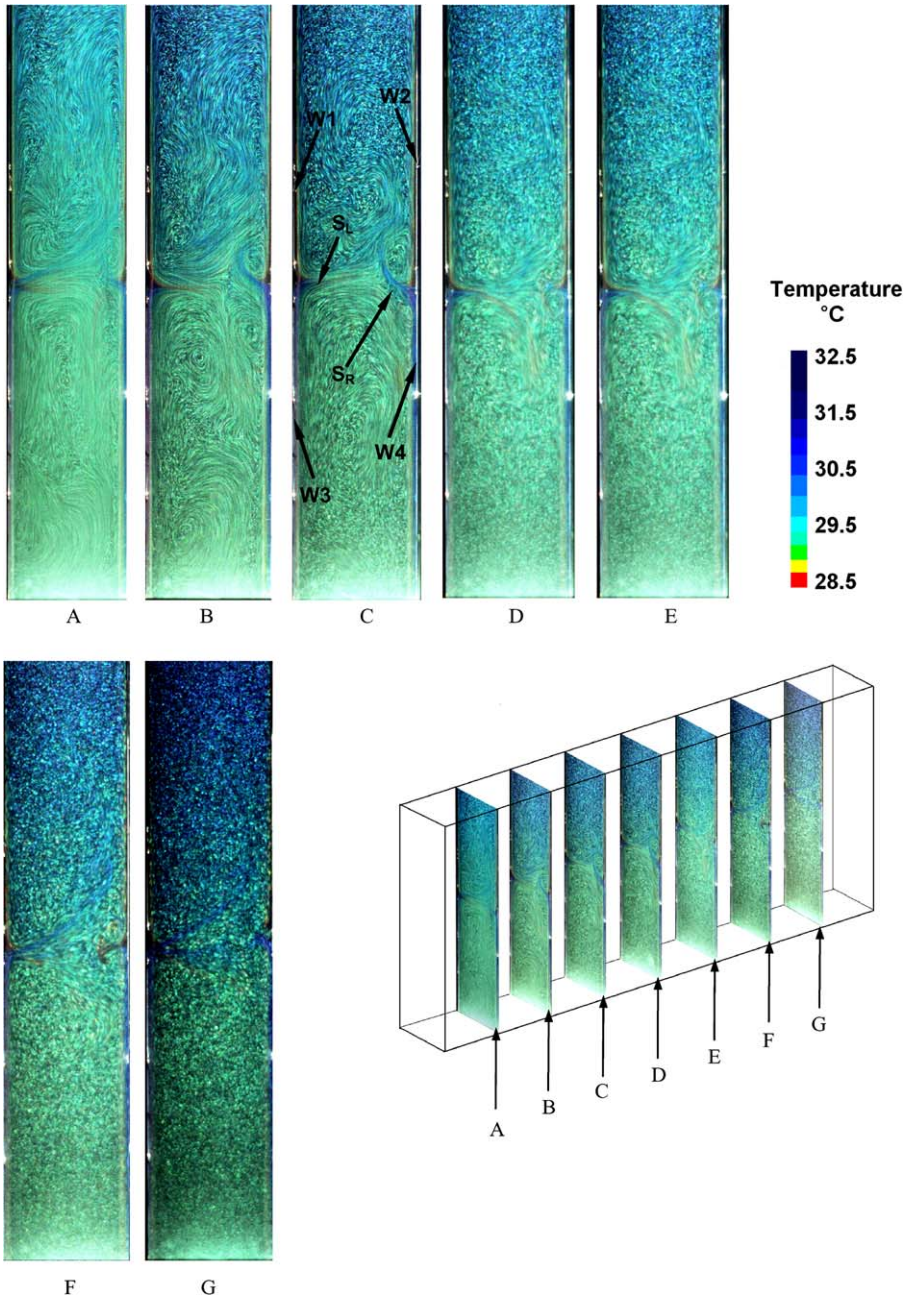

Fig. 7. Original raw color images in sequential cross-sections of the enclosure. Flow structure and temperature distributions are visualized with TLC particles: (A) $z = 0.075$ m, (B) $z = 0.05$ m, (C) $z = 0.025$ m, (D) $z = -0$ m, (E) $z = -0.025$ m, (F) $z = -0.05$ m, (G) $z = -0.075$ m.

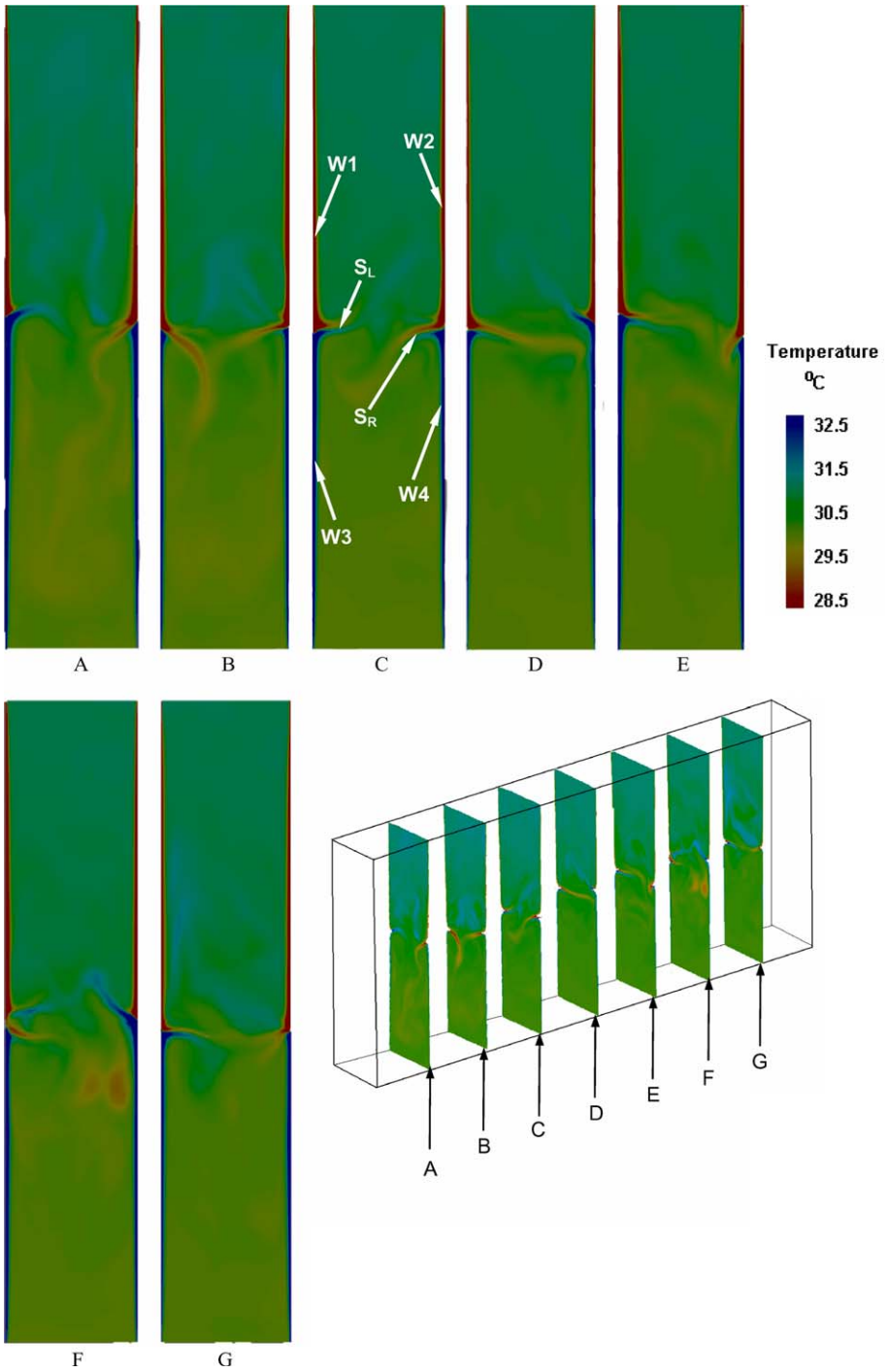

Fig. 8. Numerically simulated temperature in various cross-sections in the enclosure: (A) $z = 0.075$ m, (B) $z = 0.05$ m, (C) $z = 0.025$ m, (D) $z = -0$ m, (E) $z = -0.025$ m, (F) $z = -0.05$ m, (G) $z = -0.075$ m.

and B), because light from the planes in the back has to travel a longer distance through the fluid and gets affected by diffraction and diffusion.

The wall-layers on the upper sidewalls have lower temperatures when compared with the temperatures of the wall-layers on the lower sidewalls. High temperature gradients are localized mainly in the near-wall regions. One noteworthy and somewhat counterintuitive feature is that the temperature in the upper-half core region is higher than the temperature in the center core of the lower-half; this temperature distribution is thus inverted when compared to the specified wall temperatures. This reversed distribution can be explained by the fluid exchange structure at the median height region where the wall-layers collide head-on.

A detailed enlargement color photograph at the median height in the $Z0$-plane is shown in Fig. 9. The wall-layers W1 and W3 collide, join and mix with each other, and form

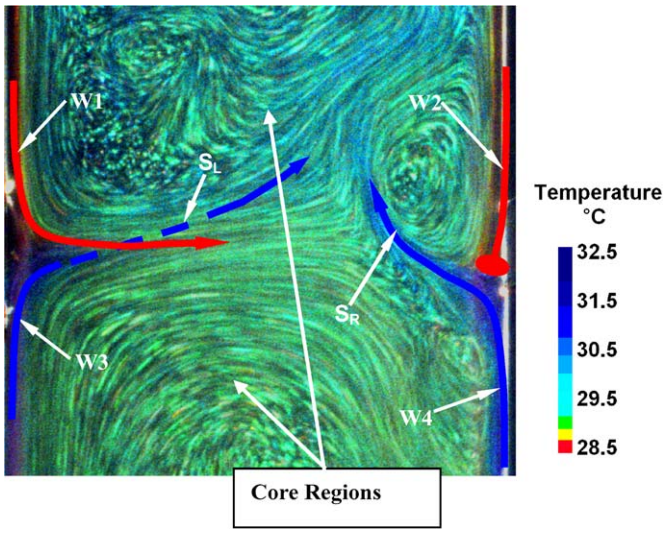

Fig. 9. Image of the visualized temperature distribution and flow structure in the median section region. W1 and W2 are the downward moving wall-layers. W3 and W4 are the upward moving wall-layers. S_L and S_R are the streams formed by wall-layers.

a stream that flows into, and entrains the center region. During the mixing, the high temperature fluid tends to flow upward while lower temperature fluid heads downward. Wall-layers W2 and W4 have a different collision pattern. Thus, W4 keeps its direction and flows into the upper-half, while wall-layer W2 flows into the lower half by turning in the z-direction. After collision, wall-layer W2 is out of the $Z0$-plane and cannot be observed from Fig. 9. An inspection of the TLC color variation at the location of wall-layer collisions indicates the existence of strong vertical temperature gradients, most likely contributing to flow momentum in that direction. In the center region between the wall-layers at the median height, temperature gradients exist in all three directions and are to a great measure responsible for the three-dimensional unsteady mixing. Just like in the case of the velocities, the temperature distribution is unsteady.

The temperature gradients take different orientations in different regions of the enclosure. Thus, in the wall-layers the temperature gradient is horizontal, while in the region where the wall-layers collide head-on with each other, the temperature gradient is vertical. In the median height region, and in-between the wall-layers, the direction of the temperature gradient is changing due to the unsteady mixing of the streams.

This natural convection flow, as it is driven by temperature variations, behaves as a function of the temperature gradient directions. In the region where the wall-layers collide head-on (at the median height region), the temperature gradient is oriented vertically and inverted (lower temperature in the upper- and higher temperature in the lower half). In this region the flow instability comes into play due to the higher temperature fluid trying to rise upward, while the lower temperature fluid is penetrating downward.

5.4. Flow in the wall-layers

The four wall-layers take only about five percent of the space in the enclosure, but their strength and the interaction between the respectively adjacent ones determine the overall stream flow characteristics in the enclosure. The wall-layers start flowing downward at the top edge of the upper side-walls and upward at the bottom edge of the lower-half side-walls, respectively. As the wall-layers flow towards the median height, their thickness increases since fluid from the central core region is entrained into the wall-layer. As already described, at the median height plane, the wall-layers from the upper walls and from the lower walls collide head-on with each other. The collision either merges the two wall-layers together or redirects them in the third z-direction. The fluid from the upper wall-layers then fills mainly into the lower-half and the fluid from the lower wall-layers fills the upper core.

The nature of the wall-layers, as viewed through their velocity and temperatures profiles, is absolutely critical to the overall flow structure. It is noteworthy that, instead of being driven by the total temperature difference, ΔT, the wall-layers are driven by the temperature difference between the wall temperature and the temperature of the cores. In turn, the temperature of the core itself depends essentially on the flow structure of the streams, the nature of their collisions at the median height, and the fluid exchange between the two halves.

Fig. 10 shows both the experimental points and the simulation results for the velocity and temperature fields in the near-wall regions. The experimental uncertainty for the flow velocity is ± 0.2 mm/s, resulted mainly from the particle tracking procedure in determining the center of the particles on the recorded flow images. For the temperature data obtained from the TLC particles, the uncertainty lies in $\pm 6\%$ range. From an inspection of the figure, one can see that the agreement between the quantitative numerical and experimental results is rather good. One has to emphasize that the steady nature of the wall-layers is instrumental for the good coincidence of the quantitative agreement. One can see from the inspection of the velocity profile that on the wall surfaces the velocity is zero. Away from the wall, the velocity is steady, downward on the upper walls and upward on the lower ones (not shown in the figure). In the center region, the flow is moving upward in the upper-half and downward in the lower-half. In the near-wall region there is a local maximum velocity which also represents an inflection point in the velocity profile and delineates the actual thickness of the wall-layer. Thus, the latter can be defined as the region between the wall surface and the location of the local maximum velocity. The thermal wall-layer occupies the region bounded by the wall surface and the isotherm of $(T - T_L)/(T_H - T_L) = 0.5$. One has to note again that beyond the wall-layer region, the velocity magnitudes are affected by the complicated central flow where the core has become unsteady. The temperatures of the fluid in the center core regions, Fig. 10b, are

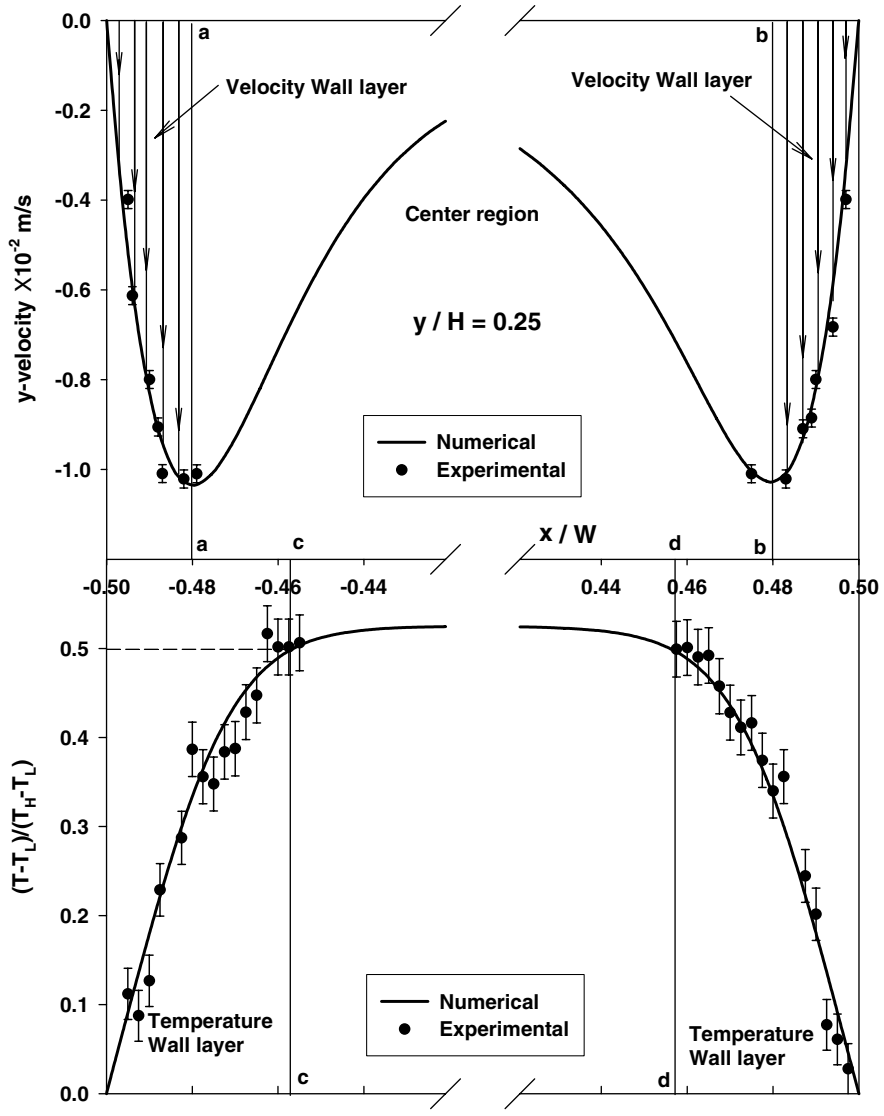

Fig. 10. Velocity and temperature distributions across the wall-layers in the $Z0$-plane at the mid-height of the upper chamber ($y/H = 0.25$) and the definition of wall-layer thickness.

close to the average of T_H and T_L. The temperature fields (experimental and numerical) indicate that very large temperature gradients exist in the vicinity of the wall; the largest portion of the temperature gradient is mainly contained in the visible layer near the wall (Figs. 7 and 9). In the core region bounded by the thermal wall-layers, the fluid temperature is close to uniform even though flow mixing and fluctuations do exist.

Another parameter of the wall-layer flow is its thickness. In Fig. 11 we have plotted the wall-layer thickness with respect to its position along the walls. The distance between the wall-layer outer edge and the wall surface ($x - x_w$), where x_w is the x-location along the wall, is non-dimensionalized with respect to the enclosure width, W. The two pairs of wall-layers, for the two pair of walls, are identical in both velocity magnitude and wall-layer thickness. At the median height, the head-on collision of the lower layer with the upper one affects greatly the local thickness. In Fig. 10a we are also showing the calculated change in the boundary layer thickness, for a vertical plate immersed in an infinite fluid (the dash-dot line). In the case of the experiment presented herein the wall-layer is exposed to a quite dynamic and unsteady central core region that compresses the wall-layers and confines them closer to the wall.

The thickness of the thermal wall-layer has a similar distribution as the momentum wall-layer, but is roughly twice as thick, Figs. 10 and 11B. Just like the momentum wall-layer, at the median height region, the thermal wall-layer is thicker (much thicker than the velocity one) because of the head-on collisions, the additional convective heat transfer and the mixing of the fluid from the two wall-layers. One should again note the good coincidence between the experimental results and the numerical simulation.

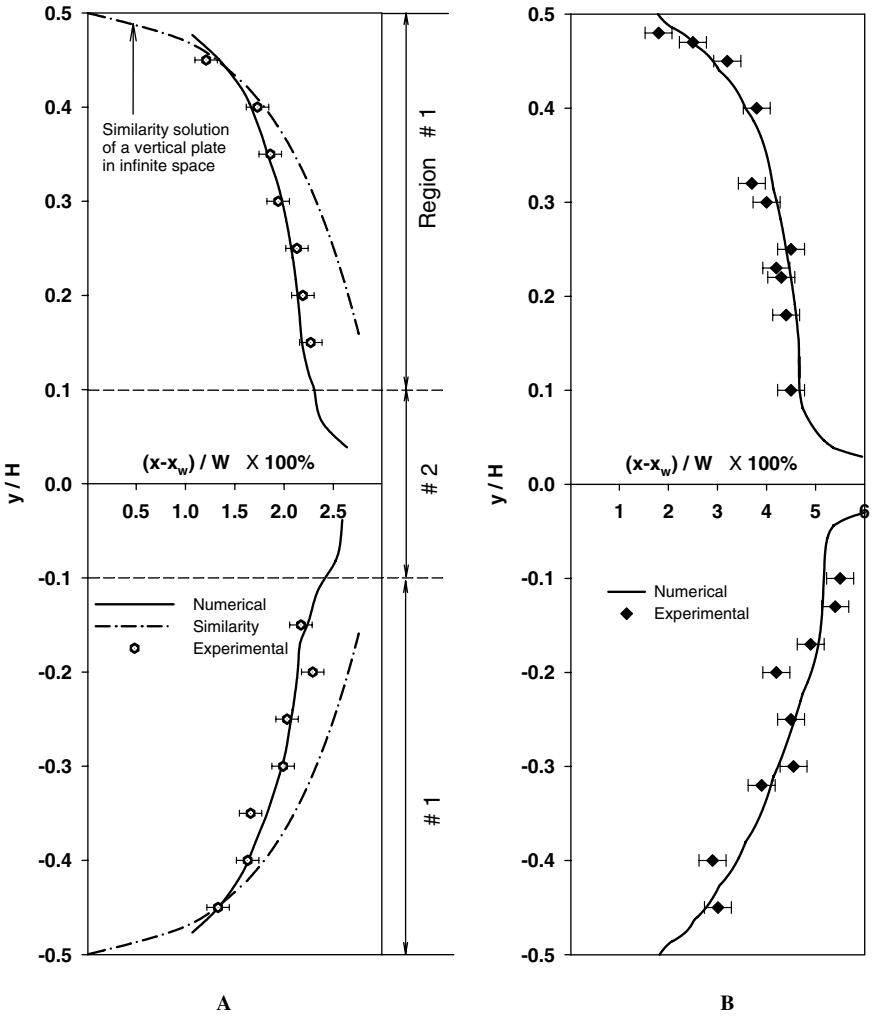

Fig. 11. Distributions of the wall-layer thickness along the walls and the two regions of the wall-layer: (A) velocity wall-layer and (B) temperature wall-layer.

5.5. Flow in the core region

The unsteady core regions bounded by the wall-layers occupy more than ninety percent of the total volume of the enclosure. In order to obtain the stream fluctuation information, velocity and temperature data were recorded at various points during the numerical simulation. These geometric points include the center of the upper half ($x/w = 0$, $y/H = 0.25$, $z = 0$), the center of the enclosure ($x = 0$, $y = 0$, $z = 0$), and the center of the lower half ($x/w = 0$, $y/H = -0.25$, $z = 0$). Fig. 12A shows the fluctuations of the three velocity components (u, v, w) at the center of the upper-half, while Fig. 12B shows the velocity fluctuations, but at the center of the enclosure. In Fig. 12A, the three velocity components have roughly the same fluctuation frequency and the magnitudes. One can say that the fluctuation is isotropic. However, at the median height the flow is dominated by the interaction of the two streams S_L and S_R. As one can see, the fluctuation of the u-velocity has much higher magnitude when compared to the fluctuations of the v- and w-velocities. In other words, the fluctuation is anisotropic.

One can see that flows in the wall-layers and in the center core have different characteristics. In the numerical simulation of the flow, two parameters (heat flux and velocity fluctuation) that characterize the flows were selected to judge the grid convergence. One should not select one overall parameter, since the latter may be dominated by the flow in one region or another. In the cases studied in this paper the total heat flow rate from the lower sidewalls to the upper sidewalls (an overall parameter) is dominated by the wall-layer flows and thus not appropriate to alone indicate numerical convergence.

5.6. Fluid exchange between the two halves

The fluid exchange mechanism between the two halves at the median height is the main focus of the study and it is very important for flow management in hydrothermal vessels. For instance, in the crystal growth industry, the exchange of fluid between the two halves is instrumental in the transport of crystal material from the lower half to the upper one where actual crystallization occurs.

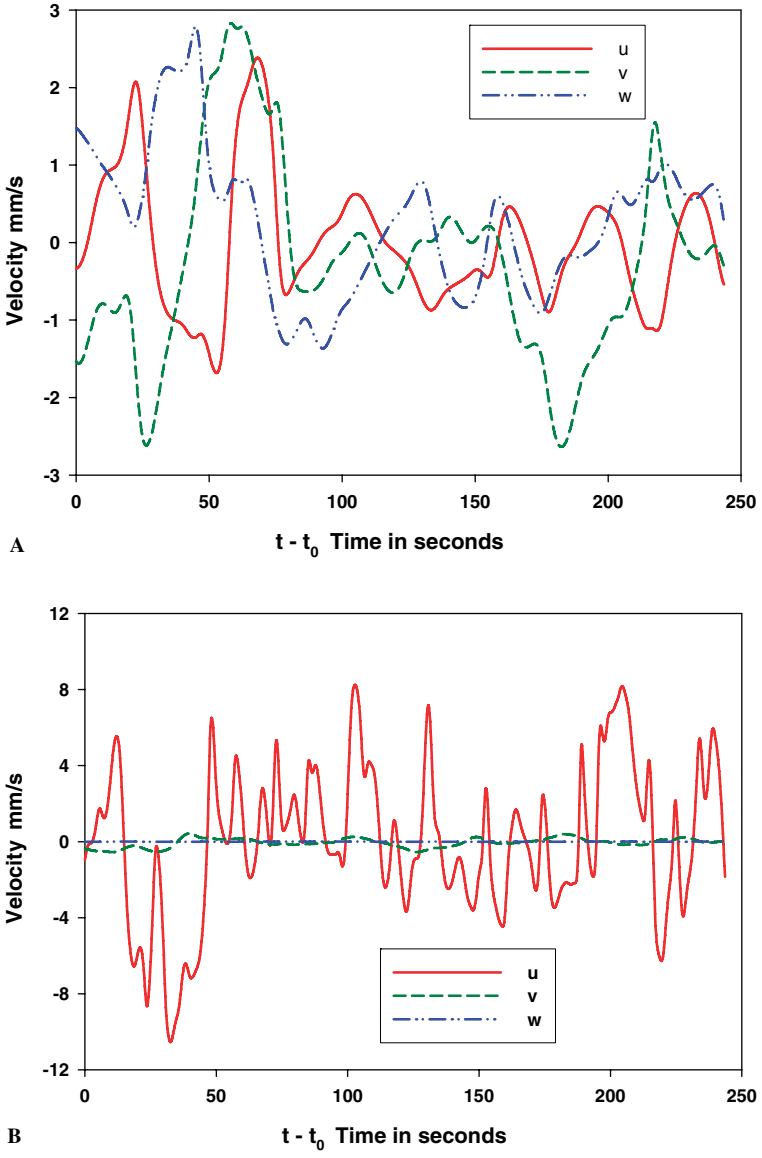

Fig. 12. Velocity fluctuations in the core region: (A) at the center of the upper half ($x = 0$, $y = H/4$, $z = 0$) and (B) at the center of the enclosure ($x = 0$, $y = 0$, $z = 0$).

Fig. 13 plots a three-dimensional flow structure on three horizontal cross-sections (y-planes): (a) the middle plane of the upper half ($y/H = 0.25$), (b) the median height plane ($y/H = 0$), and (c) the middle plane of the lower half ($y/H = -0.25$). At the middle plane of the two halves, the wall-layers and the core streams region can be clearly recognized. In the near-wall region at the median height ($y/H = 0$), an unstable temperature gradient can be observed. As a result of the unstable temperature distribution, high temperature fluid from the lower half tries to rise up, and low temperature fluid located in the upper-half streams downward. At some locations, flow is upward while at others it is downward. The velocity magnitude and the direction of the flow at all locations are changing with time. The flow direction is determined mainly by the interaction and the relative strength of the upward and downward wall-layers at that location. Either upward, or downward, the flow crossing the median height plane represents the fundamental fluid exchange mechanism between the two halves. The three-dimensional construction of fluid exchange structure is established by the collision between a downward wall-layer and an upward wall-layer. The stream thus formed during and after the collision is oriented towards the weaker one of the two colliding wall-layers.

5.7. Applications to hydrothermal growth

The experimental flow patterns and the quantitative flow and temperature data confirm the numerical results. This coincidence offers a validation of the numerical model proposed, which then can be used by extension to simulate

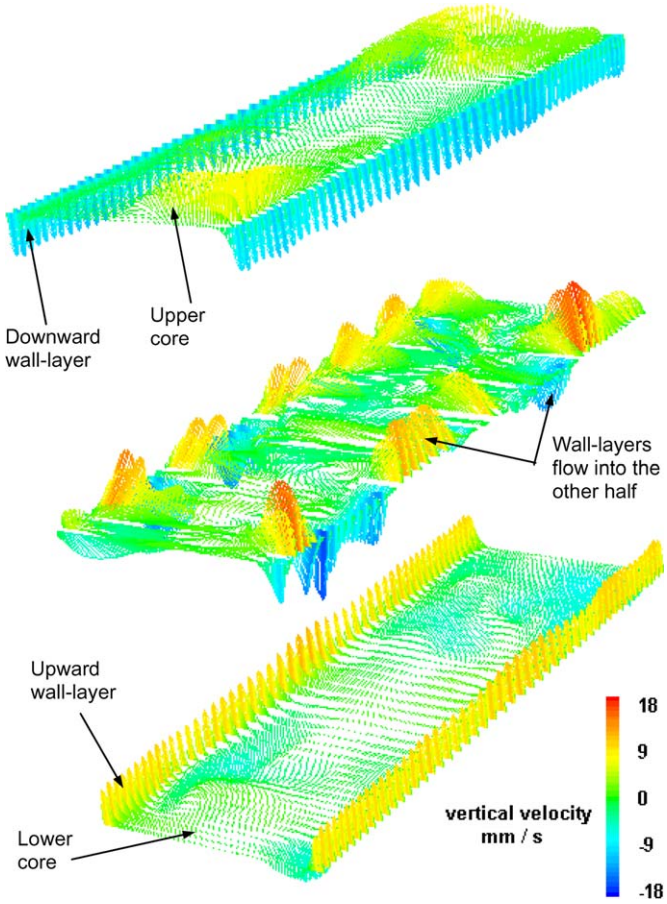

Fig. 13. Numerically obtained fluid exchange structure in the mid-section region. Velocity vectors are colored by vertical-velocity.

the thermal fluid process in autoclaves at high pressure and high temperature conditions and various Raleigh numbers in the unsteady laminar flow regime.

The flow structure in the enclosure shows that the fluid exchange between the two halves of the test section, Fig. 2, is caused by the action and interaction of the wall-layers with the rest of the fluid bulk. Based on crystal growth industry experience and previous research efforts, it is known that a large amount of fluid exchange between the two halves is detrimental to the thermal environment in the growth region. In industry autoclaves a deflecting baffle, a plate with an opening at the center, is used to separate the two halves. However, there is always a gap between the baffle and the sidewall of an autoclave. The effects of this gap were neglected in all previous numerical investigations. The findings in this paper affirm that the interaction between the wall-layer and large amounts of fluid exchange are still possible through such a gap. In order to achieve a better growth environment, the autoclave designers should make the gap as small as possible.

Wall-layers form on both the lower- and upper-wall surfaces. Most of the temperature changes occur in the wall-layer flow, even though it occupies only 5% of the whole volume of the enclosure. As it is known that large temperature gradients cause significant growth defects in the crystals, crystal growers should avoid mounting crystals close to the wall-layers and design the autoclave bodies in such sizes that the crystal seeds will, at all times, be at significant distance from such wall-layers.

As the Rayleigh number increases, the fluctuation frequency of unsteady natural convection flow structures increases with it. The results presented herein show that the flows in the center region are already unsteady at Rayleigh numbers of the order of 10^7. That leads clearly to the conclusion that at higher Rayleigh numbers the bulk flow will be highly unsteady. With such an unsteady flow, the growth environments surrounding the crystal seeds vary with time. The local spatial and temporal effects in the variation of the temperature and flow velocity of the growth environment (and with them of the mass transfer), greatly affect the quality of the resulting crystals. Until the work presented herein, these variations have not been studied in detail because previous efforts are either in steady laminar flow regime or highly turbulent flows. The former does not involve flow and temperature variation with time, and in the latter the models used offered only time averaged turbulent representations. Thus, in designing an autoclave and choosing a growth process, autoclave designers and crystal growers should also consider the local temperature variation and flow unsteadiness together with the time-averaged temperature and velocities.

6. Conclusions

The flow and temperature in an enclosure of aspect ratio 4.8 with 4 °C flow driving temperature differential between the lower half and the upper half walls are experimentally visualized and numerically simulated. The observed flow structure includes four wall-layers which occupy only 5% of the space in the enclosure, and the center core region that occupies the rest of the volume. In the wall-layers, flow and temperature are steady. The velocity distribution across the wall-layer and the wall-layer thickness along the walls are presented. Core stream flows are unsteady and three-dimensional. In the median section of the enclosure the wall-layers collide head-on, and the core streams structure and flow direction is governed by the relative strength of the wall-layer flows. Core streams, either in the upper- or the lower-halves, carry out the fluid exchange between the two halves. Flow fluctuations in the center region are found to be homogenous in the top and bottom parts, while dominated by the horizontal velocity in the median height region. The flow in the enclosure has two distinct regions and each one of them has its own flow characteristics and governing parameter. Both parameters, rather than one overall parameter (as practiced until now), should be selected for grid convergence study, as it has been implemented here.

The material presented in this paper first, offers the numerical practitioner an algorithm that has a proven predictive capability with the confidence gained from the validation of the numerical results through our own original

experiments. Secondly, with the fundamental understanding of the flow interaction and transport mechanism, the crystal growth industry can start to optimize heating schedules and driving temperature ranges while also improving the architecture of the autoclave to minimize the unsteady core flow, place crystal seeds far from the steep gradient layers present in the wall-layers, and redesign the mid-section separating baffles in optimal size and appropriate distance from the walls of the autoclave. Work that is presently in progress uses the same algorithm to address exactly the matter of baffle geometries and its position in the autoclave.

References

[1] I. Catton, Natural convection in enclosure, Heat transfer 6 (1978) 13–31.

[2] S. Ostrach, Natural convection in heat transfer in cavities and cells, in: Proceedings of the 7th International Heat Transfer Conference, Munich, Germany, 1982, pp. 365–379.

[3] S. Ostrach, Natural-convection in enclosures, J. Heat Transfer—Trans. ASME 110 (4B) (1988) 1175–1190.

[4] M. Ishikawa, T. Hirata, S. Noda, Numerical simulation of natural convection with density inversion in a square cavity, Numer. Heat Transfer: Part A—Appl. 37 (4) (2000) 395–406.

[5] O. Aydin, A. Unal, T. Ayhan, A numerical study on buoyancy-driven flow in an inclined square enclosure heated and cooled on adjacent walls, Numer. Heat Transfer: Part A—Appl. 36 (6) (1999) 585–599.

[6] C.H. Cheng, K.S. Hung, Numerical predictions of thermal convection in a rectangular enclosure with oscillating wall, Numer. Heat Transfer: Part A—Appl. 48 (8) (2005) 791–809.

[7] J.L. Niu, Z.J. Zhu, Numerical evaluation of weakly turbulent flow patterns of natural convection in a square enclosure with differentially heated side walls, Numer. Heat Transfer: Part A—Appl. 45 (6) (2004) 551–568.

[8] M. Rahman, M.A.R. Sharif, Numerical study of laminar natural convection in inclined rectangular enclosures of various aspect ratios, Numer. Heat Transfer: Part A—Appl. 44 (4) (2003) 355–373.

[9] M.M. El-Refaee, M.M. Elsayed, N.M. Al-Najem, A.A. Noor, Natural convection in partially cooled tilted cavities, Int. J. Numer. Methods fluids 28 (3) (1998) 477–499.

[10] M.D. Impey, D.S. Riley, On exchanges between convective modes in a slightly tilted porous cavity, Math. Proc. Cambridge Philos. Soc. 110 (Part 2) (1991) 395–416.

[11] H. Li, M.J. Braun, Flow structure and transport mechanism in lower half heated upper half cooled enclosures in laminar flow regime, Heat Mass Transfer, in press.

[12] H. Li, M.J. Braun, E.A. Evans, G.X. Wang, G. Paudal, J. Miller, Natural convection flow structures and heat transfer in a model hydrothermal growth reactor, Int. J. Heat Fluid Flow 26 (1) (2005) 45–55.

[13] M. Lighthill, Theoretical consideration on free convection in tubes, Quart. J. Mech. Appl. Math. 6 (4) (1953) 398–439.

[14] D. Japikse, E. Winter, Heat transfer and fluid flow in the closed thermosyphon, Heat transfer 1970, in: 4th International Heat transfer Conference, Paris-Versailles, 1970, NC 2.9, pp. 1–11.

[15] G. Mallinson, A. Graham, G.de V. Davis, Three dimensional flow in a closed thermosyphon, J. fluid Mech. 109 (1981) 259–275.

[16] H. Li, E.A. Evans, G. Wang, Flow of solution in hydrothermal autoclaves with various aspect ratios, J. Cryst. Growth 256 (1–2) (2003) 146–155.

[17] H. Li, E.A. Evans, G.X. Wang, A three dimensional conjugate model with realistic boundary conditions for flow and heat transfer in an industry scale hydrothermal autoclave, Int. J. Heat Mass Transfer 48 (25–26) (2005) 5166–5178.

[18] H. Li, G. Wang, E.A. Evans, Three-dimensional flow of solution in an industry-size hydrothermal autoclave subjected to non-uniform heating—effects of a baffle on flow and temperature separation, J. Cryst. Growth 271 (1–2) (2004) 257–267.

[19] V.A. Kuznetsov, A.N. Lobachev, Hydrothermal method for the growth of crystals, Soviet Phys.—Crystallogr. 17 (4) (1973) 775–804.

[20] R.A. Laudise, The Growth of Single Crystals, Prentice-Hall, Inc., Egnlewood Cliffs, NJ, 1970.

[21] M.J. Braun, V.A. Canacci, L.M. Russell, Full field flow visualization and computer-aided velocity-measurement in a bank of cylinders in a wind-tunnel, Exp. fluids 13 (2–3) (1992) 117–127.

[22] M.J. Braun, F.K. Choy, C.H. Moore, S.B. Lattime, A hue based computer automated method for non-intrusive temperature evaluation using thermochromic liquid crystals, in: Imaging in Transport Processes, Begell House Inc., 1993, pp. 157–169.

[23] M.J. Braun, R.C. Hendricks, V. Canacci, Non-intrusive qualitative and quantitative flow characterization and bulk flow model for brush seals, in: Proceedings of the Japan International Tribology conference, Nagoya, Japan, 1990, pp. III 1611–1616.

[24] M.B. Dzodzo, M.J. Braun, S.B. Lattime, A non-intrusive computer automated investigation of natural convection using thermochromic liquid crystals and comparison with numerical simulation, in: Proceedings of the tenth international heat transfer conference, 1994, vol. 2, Paper #2-MT-6, pp. 225–230.

[25] S.B. Lattime, Thermochromic liquid crystal applications in a quantitative study of laminar natural and forced convection heat transfer, Master thesis, The University of Akron, Akron, OH, 1995.

[26] P.T. Ireland, T.V. Jones, Response time of surface thermometer employing encapsulated thermochromic liquid crystals, J. Phys. E: Sci. Instrum. 20 (10) (1987) 1195–1199.

[27] R. Wiberga, N. Lior, Errors in thermochromic liquid crystal thermometry, Rev. Sci. Instrum. 75 (9) (2004) 2985–2994.

[28] J.W. Baughn, M.R. Anderson, J.E. Mayhew, J.D. Wolf, Hysteresis of thermochromic liquid crystal temperature measurement based on hue, J. Heat Transfer—Trans. ASME 121 (4) (1999) 1067–1072.